Geomech. Geophys. Geo-energ. Geo-resour. (2021) 7:101
https://doi.org/10.1007/s40948-021-00295-w

ORIGINAL ARTICLE

An effective dual-medium approach to simulate microwave heating in strongly heterogeneous rocks

Tianyu Chen · Wei Xiong · Guanglei Cui · Hongwen Yu · Derek Elsworth · Bobo Shi · Xiating Feng · Zhejun Pan

Received: 16 February 2021 / Accepted: 18 September 2021 / Published online: 23 October 2021

Abstract Microwave irradiation is widely applied as a heating method since this approach avoids the intrinsic limitations of heat transfer via conduction. However, microwave heating in highly heterogeneous materials, such as rocks, remains poorly understood. Current approaches applied to rocks typically ignore (i) state transformations of liquid and solid, (ii) impacts of the temperature-dependent dielectric permittivity and specific heat capacity, and (iii) innate microscale mineral heterogeneities in the evolution of temperature within mineral aggregates. We address these limitations with a dual-component effective-medium approach. In this approach, mineral aggregates in the shale matrix are separated into high- and low-transformative-capability materials (HTC and LTC systems), coupled by heat transfer. The temperature increase in the HTC and LTC systems is affected by both microwave irradiation and heat transfer. The temperature differential between these two systems increases with increasing irradiation time, and heat transfer acts to ameliorate this differential. A three-stage temperature-evolution profile is replicated for rocks comprising linearly increasing, stable and rapidly increasing stages. The peak in the specific heat capacity-temperature curve is the main contributor to the plateau stage. Additionally, in the case of a high heat transfer coefficient, all three stages can be observed in both systems, while in the case of a low heat transfer coefficient, not all three stages occur. The impact of the real part of the dielectric permittivity is not universal, while a higher value of the imaginary part results in a larger increase in temperature. This work proposes an alternative approach to simulate the microwave heating process in heterogeneous materials.

Highlights

- Mineral aggregates in the rock matrix are separated into high- and low-transformative capacity systems, coupled by heat transfer.

T. Chen (✉) · G. Cui · H. Yu · X. Feng
Key Laboratory of Ministry of Education on Safe Mining of Deep Metal Mines, Northeastern University, Shenyang 110004, China
e-mail: chentianyu@mail.neu.edu.cn

W. Xiong
Coal Technology and Engineering Group Crop., Chongqing Research Institute of China, Chongqing 400037, China

D. Elsworth
Department of Energy and Mineral Engineering, G3 Center and Energy Institute, The Pennsylvania State University, University Park, PA 16802, USA

B. Shi
State Key Laboratory of Coal Resources and Safe Mining, China University of Mining and Technology, Xuzhou 221116, China

Z. Pan
CSIRO Energy Business Unit, Private Bag 10, Clayton South, VIC 3169, Australia

- A dual-component effective-medium approach considering the above two systems is proposed to simulate the microwave heating process in heterogeneous rocks.
- A three-stage temperature-evolution profile is replicated for rocks comprising linearly increasing, stable and rapidly increasing stages.

Keywords Mineral aggregates · Phase transition · Specific heat capacity

1 Introduction

Microwave irradiation is a widely applied heating method, primarily due to its notable advantages over conventional conductive and radiative heating techniques (Farag et al. 2012; Liu et al. 2018). In areas related to rock mechanics, this method is mainly applied in rock breakage (Hartlieb et al. 2012; Lu et al. 2017; Yu et al. 2021), drilling (Jerby et al. 2002), grinding (Kingman et al. 2000), leaching (Wen et al. 2017), and unconventional gas/oil recovery (Hascakir and Akin 2009; Bera and Babadagli 2017; Cui et al. 2020a). Rock microwave heating has been frequently explored since the 1980s (McGill et al. 1988; Ulaby et al. 1990), while the mechanisms in highly heterogeneous rocks remain unclear.

Most rock types encountered in the Earth crust have been heated to examine variations in temperature and mechanical and dielectric properties through microwave irradiation, such as granite (Li et al. 2020; Deyab et al. 2021) and basalt (Yuan et al. 2020). As observed in these works, the temperature increases with the irradiation time but is highly dependent on the rock types. The microwave heating process of rocks can be divided into three stages with increasing temperature, and the rock response of each component is different. During the first period, the temperature increases linearly with the irradiation time over the short term in most rock types (Peinsitt et al. 2010; Chandrasekaran et al. 2013; Hartlieb et al. 2018). Following this period, the temperature remains nearly constant as irradiation continues. During this period, all absorbed electromagnetic power contributes to water evaporation or mineral phase conversion (Bobicki et al. 2014; Nicco et al. 2018). During the third period, the temperature again increases once all water has evaporated or mineral conversion has been completed (Pickles 2004; Liu et al. 2016). Whether each of these three periods occurs depends on the electrical and thermodynamic parameters of the rocks and mineral aggregates. Li et al. (2020) and Deyab et al. (2021) observed only the first period during microwave heating of granite. Without a fundamental understanding of the underlying mechanisms of the microwave heating process in heterogeneous rocks, researchers have not quantifiably evaluated the induced rock breakage process.

Rock is a highly heterogeneous material comprising many different minerals with differing responses to microwave irradiation (Tahmasebi et al. 2011; Li et al. 2019a): (i) microwave transparency, (ii) microwave absorption, and (iii) both microwave reflection and absorption. Both rapidly and slowly heating minerals typically coexist within a given rock type, where irradiation is absorbed by minerals with a high dielectric loss and passes through those minerals with a low dielectric loss or microwaves are totally reflected (Haque 1999; Jones et al. 2002). As a pioneering and fundamental work, Ford and Pei (1967) microwave-heated 17 compounds and found that dark colored minerals were rapidly heated, while a longer exposure time was required for light colored minerals. A comprehensive investigation was conducted by Chen et al. (1984), in which 40 minerals were subjected to microwave heating. These earlier works emphasized mineral processing instead of rock-forming minerals. Eleven basic rock-forming minerals were microwaved by Lu et al. (2017) with a mutimode microwave instrument, and enstatite exhibited a high microwave adsorption capacity, while the other minerals exhibited a low adsorption capacity. Based on their observations, the microwave-adsorbing minerals included plagioclase, pyroxene, ilmenite, enstatite and biotite, and the poorly microwave-adsorbing minerals included quartz, orthoclase, calcite, albite, feldspar, and muscovite.

The microwave heating-related parameters of different minerals have also been widely characterized. The dielectric permittivity is generally employed to characterize the capacity of mineral aggregates to interact with electromagnetic waves (Meisels et al. 2015; Toifl et al. 2016). There are several approaches to determine the dielectric permittivity of minerals. The resonant cavity perturbation approach was employed by Cumbane (2003) to investigate the dielectric properties of 11 minerals including silicates,

metal oxides and sulfides. A similar approach was adopted by Zheng et al. (2005) to determine the dielectric properties of certain minerals and rocks. Moreover, the dielectric permittivity is not a constant but varies with the temperature. The dielectric permittivity of most minerals, such as pyrite, gradually increases with the temperature (Jones 2005; Flesoura et al. 2019), while that of other minerals exhibits a sudden increase over time (Lovás et al. 2010). The specific heat capacity (C_p) is also an important parameter in describing the microwave heating process and defines the temperature (T) increase related to a given energy input. The specific heat capacity usually grows up with the temperature for a specific material (Jones et al. 2007). However, during mineral crystal phase transition or water evaporation, a large amount of energy is absorbed without any notable increase in temperature—represented as a peak in the C_p–T curve. For example, the heat capacity of quartz-rich rocks considerably increases when quartz is transformed from the α- to the β-phase (Hartlieb et al. 2016). The impacts of temperature-dependent properties such as the dielectric permittivity and specific heat capacity on the microwave heating process have not been frequently reported.

In tandem with experimental approaches, numerical approaches have been widely employed to assist in obtaining a greater understanding of microwave heating and the resulting rock breakage. In most previous work, the binary mineral model was widely adopted. Wang and Djordjevic (2014) established a two-dimensional circular plate model in which pyrite was embedded in calcite to investigate the microwave heating and breakage processes. Ali and Bradshaw (2010) numerically investigated the effect of microwave irradiation on a two-phase conceptual mineral ore consisting of 10% galena and 90% calcite. Similarly, a 3-D numerical model was employed by Toifl et al. (2016) to characterize the microwave heating process in inhomogeneous rocks, including transparent and absorbent phases. More recently, the microwave heating process of a rectangular 0.864 cm × 1.194 cm × 30 μm thin section comprising quartz, orthoclase, plagioclase, and chlorite was numerically examined by Li et al. (2019b). However, these discrete models cannot be applied to micro- and macromodels, as the mineral topology structure is hardly determined at these large scales. To achieve the goal of the continuum medium approach, several theoretical approaches have been applied to synthesize the dielectric permittivity of different components into that of a single equivalent composite material. In early models, the dielectric permittivity of the composite material was directly related to the volume fraction of the different components (Zakri et al. 1998; Simpkin 2010), with the relative location and texture of the different components ignored. The later Maxwell–Garnett model and its derivatives accommodated the impact of the shape and concentration of dispersed components (Yamada et al. 1982; Tuncer et al. 2001). More recently, a more reliable mixture theory has been proposed that considers the polarization of adjacent particles (Smith 1977). In the aforementioned approaches, highly heterogeneous materials such as rocks were homogenized, and differences in the electromagnetic and thermodynamic properties between the different minerals, hypothesized as the main mechanism of rock damage (Hartlieb et al. 2016; Toifl et al. 2016), were ignored.

To address these limitations, we introduce the concept of a double-porosity medium and propose an alternative approach to investigate microwave heating in heterogeneous rocks. In this approach, mineral aggregates in the shale matrix are divided into high- and low-transformative-capability (HTC and LTC systems) materials, coupled by heat transfer. The new approach is verified based on the experimentally observed temperature evolution in aggregates combined with numerical experiments to investigate parameter sensitivities.

2 Conceptual model

In this section, we introduce the conceptual model representing the microwave heating process in heterogeneous rocks as a dual-medium model.

2.1 Microwave heating process in rocks

The microwave heating process in heterogeneous rocks is characterized by varying microwave absorption capacities: one group exhibits a high dielectric permittivity and a notable capability to transform electromagnetic energy into heat and a second group with a low dielectric permittivity exhibiting a low transformative capacity. The second parameter includes two extreme cases: a given mineral is totally

microwave transparent or microwaves are entirely reflected. The first group is sensitive to microwave radiation, whereas the second group is insensitive.

An SEM image of shale is selected to illustrate the microwave heating process. The bright particles are pyrite with a high dielectric permittivity, while the surrounding gray minerals include quartz, clay, and calcite, characterized by low dielectric permittivity values. In this case, we represent the matrix as quartz, which is the dominant mineral in the shale matrix (Chen et al. 2019). The mineral aggregate occurs in a thermal equilibrium at the initial temperature T_0 ($T_p = T_q = T_0$), as shown in Fig. 1a. T denotes the temperature, and p and q denote the minerals of pyrite and quartz, respectively. When the aggregate is irradiated, the temperature of pyrite rapidly increases because of its high dielectric permittivity, while that of the surrounding quartz increases only slightly due to its low dielectric permittivity. At this stage, the temperature of pyrite is higher than that of quartz, i.e., $T_p > T_q$, as shown in Fig. 1b. At the second stage, thermal energy is transferred through conduction from high- to low-temperature zones, driven by the temperature gradient, as shown in Fig. 1c. In the final state, the heat conduction process is finished, and the temperature of the entire aggregate equilibrates as $T_p = T_q$, as shown in Fig. 1d. It should be noted that during the heat transfer process (the second process), the first process (microwave irradiation) continues, and $T_p > T_q$ always applies. A thermal equilibrium ($T_p = T_q$) may not be achieved during the period of microwave irradiation.

2.2 Continuum medium approach

In microwave heating, the mineral components can be categorized into two groups: a first group with a high transformative capacity (HTC) of the incident electromagnetic energy into heat and a second group with a low transformative capacity (LTC). The behavior of the second component group includes two extreme responses: minerals that are either totally microwave transparent or totally microwave reflective. In this study, the first component group is sensitive to microwave heating, while the second component group is insensitive. The microwave heating process is directly analogous to the gas injection process in porous-fractured rocks, but the microwave susceptibility and thermal conductivity are the controlling properties rather than the gas storage capacity and permeability, respectively. Similarities between the dual-porosity response during both gas injection into porous fractured rocks and microwave heating of highly heterogeneous rocks are clearly observed, as indicated in Table 1.

In the continuum approach, the mineral aggregate system is divided into HTC and LTC components with an appropriate length scale (representing the texture) and an appropriate heat transfer coefficient linking these component groups. In the calculation process, each computing node represents the surrogate temperatures in both the HTC and LTC systems linked by heat and mass transfer.

3 Mathematical model

We describe a mathematical model and governing equations capturing the coupling process of heat transfer and electromagnetic field propagation.

3.1 Microwave heating of mineral aggregates

3.1.1 Heat transfer in the HTC or LTC components

In this work, (1) the coupling process between thermal and mechanical energy is ignored and (2) the presence of fluids is neglected, microwave-induced heating adheres to the modified Fourier law of heat conduction as follows (Zhang et al. 2016):

$$\rho_i C_i \frac{\partial T_i}{\partial t} + \nabla \cdot q_i = Q_{htr} + Q_{wave-i} \tag{1}$$

where ρ_i denotes the density of the HTC or LTC minerals, kg/m^3 ($i = h$ or l, respectively); C_i denotes the specific heat capacity of the HTC or LTC minerals, J/(kg*K); T_i is the temperature of the HTC or LTC minerals, K; and $Q_{wave\text{-}i}$ is the heat source induced by microwave dissipation in the HTC or LTC minerals, J/(m^3*s). Based on the calculation of the electromagnetic loss, the heat source ($Q_{wave\text{-}i}$) may be calculated as (Jiajia et al. 2015; Li et al. 2019a):

$$Q_{wave-i} = \frac{\omega \varepsilon_0 \varepsilon'' |\mathbf{E}|^2}{2} \tag{2}$$

where ε_0 represents the permittivity in vacuum and ε'' represents the imaginary part. Furthermore, **E**

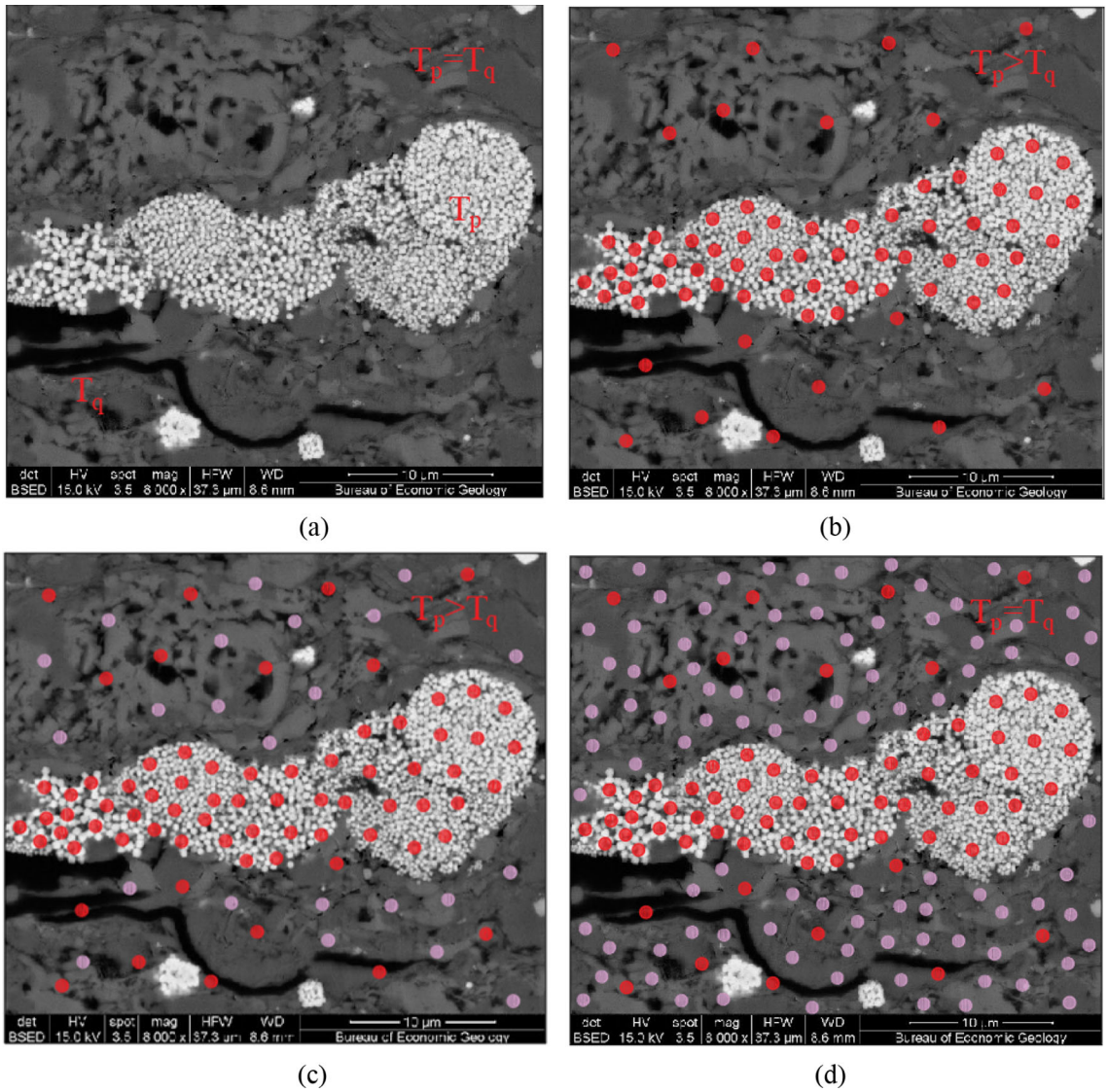

Fig. 1 Illustration of microwave heating in rock aggregates using overprinted SEM images (https://www.jsg.utexas.edu/microbeam/novanano/). **a** Initial preheating state; **b** first irradiated state; **c** continued heating and **d** final thermal equilibrium state. The red dots indicate the absorption of microwave energy, and the purple dots indicate the transfer of thermal energy via conduction

represents the electric field, V/m, which can be obtained from Maxwell's equation; $\omega = 2\pi f$ is the angular frequency, rad/s; and f is the frequency, Hz. The heat flux q_i, J/(m^2*s), is expressed as:

$$q_i = -k_{Ti}\nabla T_i \tag{3}$$

where k_{Ti} is the thermal conductivity of the HTC or LTC minerals, $W/(m*K)$.

3.1.2 *Heat transfer between the HTC and LTC components*

Heat transfer is driven by the temperature difference between the two systems and mainly depends on the thermal conductivity of the LTC system. Heat transfer between these two systems is proportional to the temperature difference (Cui et al. 2018a), as follows:

$$Q_{hl} = \lambda_l(T_h - T_l) \tag{4}$$

Table 1 Comparison of the gas injection and microwave heating processes in dual-porosity rock media and rock-containing minerals

Objects	Dual-porosity rock media		Rock-containing minerals	
Subsystem	Fracture system (*f*)	Matrix system (*m*)	HTC system (*h*)	LTC system (*l*)
External disturbance	Gas injection		Microwave heating	
Controlling variable	Gas pressure (*P*)		Temperature (*T*)	
Sensibility	High	Low	High	Low
Interactions	Mass transfer		Heat transfer	
Conductive medium	Gas mass		Thermal energy	
Key parameter	Permeability (*k*)		Dielectric permittivity (κ)	

where λ_l is a newly defined parameter representing the heat transfer rate between the HTC and LTC systems, J/(m^3*s*K).

3.2 Electromagnetic field propagation

Maxwell's equation is applied to describe how electric and magnetic fields generate through the charges, currents and changes in these fields (Onwude et al. 2018; Dirisu et al. 2019). The equation comprises four sub-equations as following:

$$\text{Gauss's law for electric fields}: \ \nabla \cdot E = \frac{\rho}{\varepsilon_0} \tag{5}$$

$$\text{Gauss's law for magnetic fields}: \nabla \cdot B = 0 \tag{6}$$

$$\text{Maxwell - Faraday equation}: \ \nabla \times E = -\frac{\partial B}{\partial t} \tag{7}$$

$$\text{Maxwell - Ampere's law}: \ \nabla \times B = \mu_0 \geq \left(J + \kappa_0 \frac{\partial E}{\partial t}\right) \tag{8}$$

where ∇ is the differential operator; $\nabla\cdot$ is the divergence operator; $\nabla\times$ is the curl operator; E represents the electric field, V/m; B represents the magnetic field, Wb/m^2; ρ is the electric charge density, C/m^3; ε_0 represents the permittivity of the free space (8.854187817 $\times$ 10^{-12} F/m); μ_0 represents the permeability of the free space (1.2566370614 $\times$ 10^{-6} H/m); and J is the current density, A/m^2.

3.3 Coupling process

Four physical fields are simultaneously solved in this work. These processes include the propagation of the electromagnetic field and the resulting heating processes in both the HTC and LTC systems. The coupling process is shown in Fig. 2. In this case, the electromagnetic field propagates within the HTC and LTC systems separately as a heating source driving heat transfer toward the complementary HTC and LTC systems, respectively, based on Eq. (2). As the temperature in the HTC and LTC systems changes, the electromagnetic parameters vary, thus affecting the propagation of the electromagnetic field. Heat transfer between the HTC and LTC systems is driven by the heat transfer term of Eq. (4). The electromagnetic field propagation processes in the HTC and LTC systems are considered interdependent, although polarization in one mineral aggregate affects the electromagnetic propagation process in an adjacent aggregate (reasonable simplification).

4 Numerical model and verification against experimental observations

The above coupled electromagnetic-heating model is implemented and solved in COMSOL Multiphysics® (Version 5.4) with the modeling process displayed below.

4.1 Simulation approach

The heating geometry must include both the microwave source and the heated object. A large difference in time scale exists when solving the electromagnetic

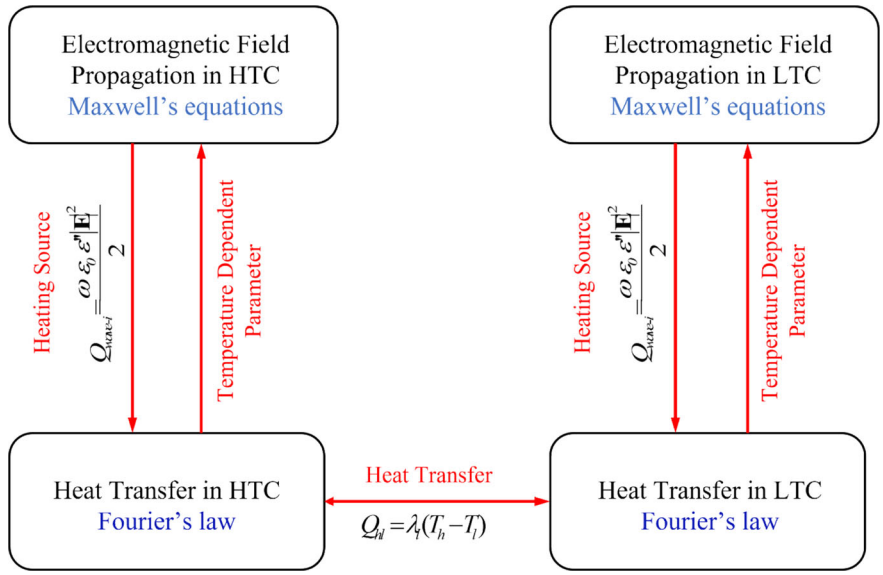

Fig. 2 Schematic of the coupling process among the different physical fields

and heating coupling process since microwave propagation involves a transient process at the timescale of nanoseconds (ns), while the heating process is a relatively slower process at the timescale of seconds (s) or minutes (min). COMSOL Multiphysics® provides a feasible approach to solve this mismatch in time scale. In this approach, Maxwell's equation is first solved in the frequency domain with the assistance of Helmholtz vector equation (Pitchai et al. 2014):

$$\nabla \times \mu_r^{-1}(\nabla \times \mathbf{E}) - k_0^2\left(\varepsilon_r - \frac{i\sigma_E}{\omega\varepsilon_0}\right)\mathbf{E}=0 \tag{9}$$

where $k_0 = \omega/c_0$ is the free-space wavenumber; c_0 denotes the speed of light in vacuum, m/s; and $\omega = 2\pi f$ represents the angular frequency. Then, the heating process is defined in a time-dependent manner through the calculated electric field (E) with Eq. (2).

In contrast to previous approaches, we divide the component minerals into the binary phases of the HTC and LTC systems. The microwave propagation and heating processes are calculated considering these two separate systems by utilizing the heating process coupled with a heat transfer term. To realize this aim, electromagnetic wave frequency domain modules are applied to each system with unique electromagnetic parameters. This approach defines the EM heating process as a result of the heating source (Eq. (2) with the heat transfer module. The heat transfer term [Eq. (4)] is then applied to each system with the same value but the opposite sign. In the calculation process, each computing node represents the state (temperature) of both the HTC and LTC systems.

4.2 Microwave heating experiment on a shale sample

A microwave heating experiment was conducted in our laboratory with a shale block collected from an outcrop categorized into Longmaxi Formation in Sichuan Province. The main component minerals include quartz, clay, and calcite, with quartz accounting for more than 30% of the shale mineral components (Chen et al. 2019), as indicated in Table 2.

In the laboratory, the shale block was prepared into a cylinder with a size of 100 mm × 50 mm(height × diameter), as displayed in Fig. 3a. A household microwave oven (Galanz, G70F20CN1 L-DG (B0), as shown in Fig. 4a) with a constant power of 700 W was employed to irradiate and heat the shale sample. The internal heating space is cuboid shaped with a size of 329 mm × 315 mm × 180 mm. A waveguide is located at the upper-right side of oven exhibiting cuboid shape (18 mm × 50 mm × 78 mm). The microwave exposure time was stepped increased. After each microwave irradiation, the sample was taken out from the oven with the temperature slowly cooled down to 90 °C (reservoir temperature). Then, the next microwave heating step was conducted with the irradiation time 30 s longer

Table 2 Mineral composition of the shale sample

Mineral composition (%)						TOC (%)	$R_{o,max}$ (%)
Quartz	Feldspar	Pyrite	Clay minerals	Calcite	Dolomite		
32.45	3.42	3.13	18.57	32.16	8.02	2.24	2.41

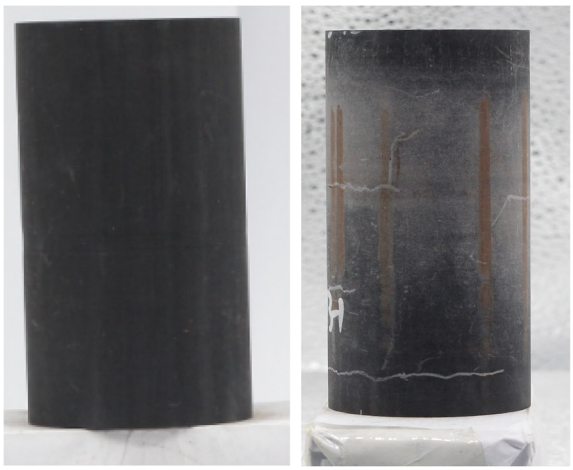

(a) (b)

Fig. 3 Image of the shale sample for the microwave irradiation experiment **a** before microwave heating and **b** after microwave heating

measured with a Fluke infrared thermometer (model: 568–2). The microwave heating process was continued for 30 min with microfractures developing, but the sample remained intact, as shown in Fig. 3b. The mechanisms contributing to microwave heating-induced fracturing have been reported in our recent studies (Cui et al. 2020a).

4.3 Numerical model

4.3.1 Geometric model

A numerical model was established with the microwave-heating module in the application library of the COMSOL Multiphysics (COMSOL 2018) platform and comprised three physical objects: a shale sample, a microwave oven, and a waveguide. The microwave oven and waveguide were both rectangular. The

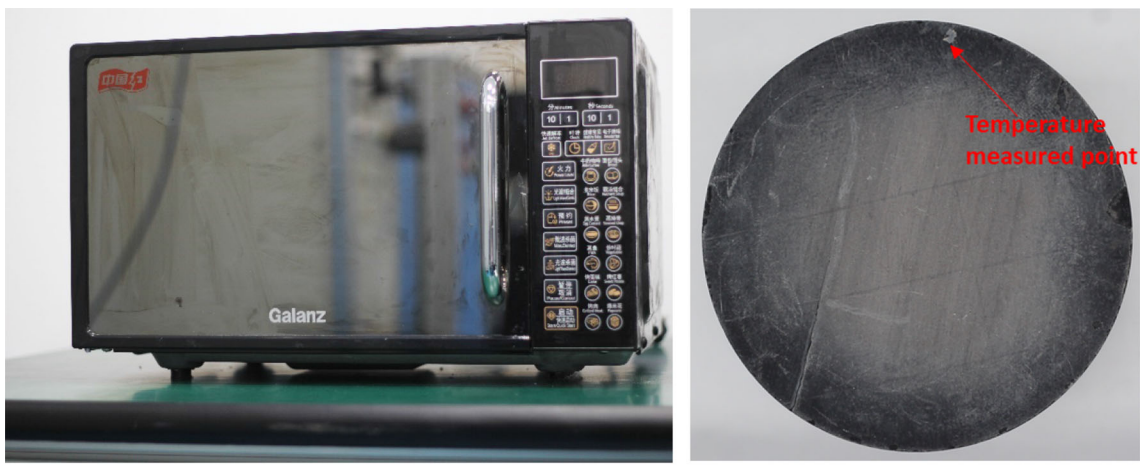

Fig. 4 Picture of **a** the household microwave oven and **b** the location of the temperature measurement point

than that in the previous step. Before and after each irradiation step, the temperature at a certain point on the upper surface of the sample (Fig. 4b) was

microwave oven was drawn as cubic shape with size of 329 mm × 315 mm × 180 mm. The waveguide exhibited a size of 18 mm × 50 mm × 78 mm. The

shale sample was cylindrical with a size of 100 mm × 50 mm(height × diameter) and rested at the center of the base of the microwave oven. The relative positions and sizes of these three objects are illustrated in Fig. 5.

4.3.2 Boundary conditions and mesh

The coupled microwave heating process was achieved with the microwave propagation process imitated in the oven and both microwave propagation and heating processes replicated in the sample. This was achieved with two electromagnetic wave modules and two heat transfer processes in the above solid models.

The boundary conditions for the electromagnetic wave modules were specified as follows: (1) an impedance boundary was employed to the oven walls of the oven to make sure the retention of all electromagnetic radiation; (2) a rectangular-shaped port boundary was defined to the entrance of the waveguide, acting as the source of electromagnetic waves at a frequency of 2.45 GHz in the TE10 mode. The cutoff frequencies for the different modules are analytically determined with the following the relationship:

$$(v_c)_{nm} = \frac{c}{2}\sqrt{\left(\frac{m}{a}\right)^2 + \left(\frac{n}{b}\right)^2} \tag{10}$$

in which m and n denote the mode numbers and c represents the speed of light. In the TE_{10} mode applied in this work, we have $m = 1$ and $n = 0$. As

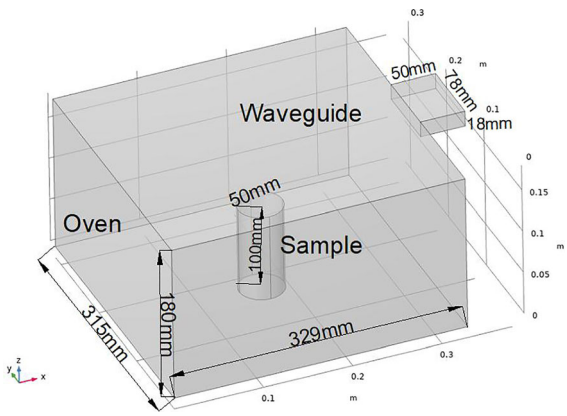

Fig. 5 Dimensions of the simulation model

defined in the geometric model, $a = 78$ mm and $b = 18$ m, the TE10 mode is the only propagating mode for frequency of 2.4 GHz.

Heat transfer in the solids module is only specified to the sample with the boundary conditions defined as follows: (1) a thermal insulation boundary condition is employed to the base of the sample; (2) a convective heat transfer boundary is assigned to all other faces. The initial temperature (ambiance temperature, T_{amb}) is 300 K.

A physically controlled mesh was employed to mesh the whole geometry. The element size was specified to fine. To obtain an accurate result, the maximum element size was refined to 1/5th of the microwave wavelength. After meshing, a total of 143,975 elements was obtained with an average element quality of 0.6623. A desktop computer with an Intel(R) Core(TM) i7-9750 CPU and 40 GB of random access memory (RAM) was used for calculation purposes.

4.3.3 Temperature-dependent parameters

The dielectric permittivity is a key parameter controlling microwave irradiation, as this parameter measures the adsorption capability of electromagnetic waves (real part) and the capacity to convert microwave energy into heat (imaginary part). The main minerals in the Longmaxi shale sample are quartz, clay, calcite, and pyrite, with quartz accounting for more than 30% of all minerals (Chen et al. 2019), as listed in Table 2. The dielectric permittivity values of pyrite and quartz vary with the temperature, as shown in Fig. 6 (Lovás et al. 2010; Zhou et al. 2011). In the case of pyrite, changes in the permittivity value occur within the temperature range from 720 to 870 K. The oxidative transformation process of pyrite into hematite ($2FeS_2 + 11/2O_2 \rightarrow Fe_2O_3 + 4SO_2$) (Corradi et al. 1996) occurring in this region could be the main cause of the sudden variation in the dielectric permittivity. The dielectric permittivity values of the other minerals are listed in Table 3 (Church et al. 1988; Zheng et al. 2005; Aqil and Schmitt 2010; Josh and Clennell 2015). The specific heat capacity (C_p) is another important parameter and defines the temperature (T) increase related to a given energy input. The specific heat capacities of the different minerals also vary with the temperature, as shown in Fig. 7, where the specific heat capacity increases with the temperature for most

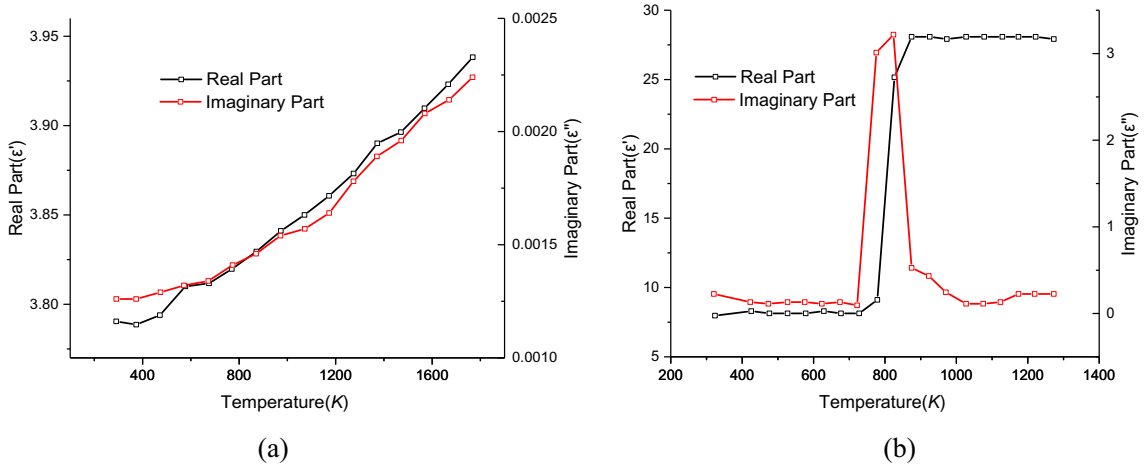

Fig. 6 Temperature-dependent dielectric permittivity of **a** quartz (Zhou et al. 2011) and **b** pyrite (Lovás et al. 2010)

Table 3 Dielectric permittivity of the minerals in the shale sample

	Quartz	Feldspar	Pyrite	Clay	Calcite	Dolomite
Real part	Figure 6a[1]	5.52[2]	Figure 6b[3]	4[4]	9.2[6]	7.41[6]
Imaginary part	Figure 6a[1]	0.01[2]	Figure 6b[3]	0.2[5]	0.005[6]	0.02[6]

1–6 are retrieved from Zhou et al. (2011), Zheng et al. (2005), Lovás et al. (2010), Josh and Clennell (2015), Aqil and Schmitt (2010) and Church et al. (1988)

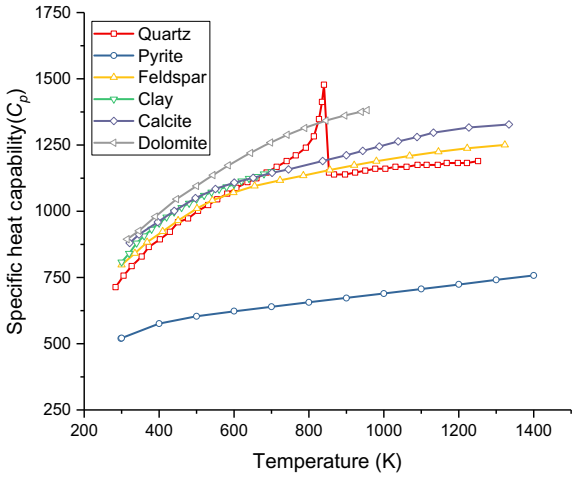

Fig. 7 Temperature-dependent specific heat capacity of the different minerals (Skauge et al. 1983; Toifl et al. 2017)

materials (Skauge et al. 1983; Jones et al. 2007; Toifl et al. 2017). In addition, a peak value for quartz due to the transformation from the α- to the β- phase was observed.

4.4 Model verification

4.4.1 Microwave heating process for the different minerals

The responses of the different minerals to electromagnetic radiation and the resulting temperatures vary because of the distinct thermodynamic parameters. In this section, the temperature changes in the different minerals with the irradiation time are investigated. During the calculation process, a small area at the center of the sample is specified to represent the different minerals with the above defined parameters applied to calculate the microwave heating process for each mineral. The average temperature in the small area is shown in Fig. 8. It should be noted that the temperature of pyrite and clay corresponds to the right axis because of the higher values, while the temperature of the remaining minerals corresponds to the left axis.

As shown in Fig. 8, the temperature increase rates are the highest for pyrite and clay compared with other

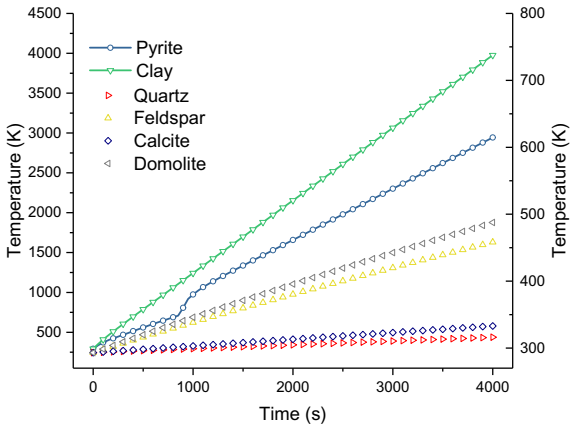

Fig. 8 Temperature changes with the irradiation time for the different minerals

minerals because of the corresponding higher permittivity value (pyrite) and lower specific heat capacity value (clay). A two-stage temperature rise is observed for pyrite attributed to the sudden increase in dielectric permittivity at approximately 700 K. In regard to the remaining minerals, the temperature increases linearly over time in the sequence of dolomite, feldspar, calcite, and quartz. Based on the above characteristics, the individual minerals are separated into two groups: pyrite and clay with higher temperature increase rates are defined as the HTC system, and the remaining minerals with lower temperature increase rates form the LTC system.

4.4.2 Verification results

In this section, temperature-dependent dielectric permittivity and specific heat capacity values are assumed for the HTC and LTC systems to match the experimental data. The value and variation in the dielectric permittivity and specific heat capacity of clay and pyrite define the HTC system. Similarly, the parameters of the LTC system are specified based on the value and variation in the dielectric permittivity and specific heat capacity of the remaining minerals. The established relationships between the assumed dielectric permittivity and specific heat capacity values and the temperature are shown in Figs. 9 and 10, respectively.

As shown in Fig. 9a, the variation in the dielectric permittivity with the temperature of the HTC system is similar to that of pyrite, while the value of the imaginary part is closer to that of clay. Both the imaginary and real parts of the dielectric permittivity of the LHC system gradually increase with increasing temperature. In regard to the variation in the specific heat capacity with the temperature, there occurs a rapid increase in the LTC system with the temperature because of the phase transition of quartz and a slow increase in the HTC system, as shown in Fig. 10.

The remaining parameters for model verification are displayed in Table 4. With the comparisons of the simulation results to experimental data are illustrated in Fig. 11. The position of the temperature measurement point in the simulation model cannot be determined. Therefore, the simulated temperature curve was measured as the average value across the top surface. In the verification process, the temperature of the LTC system is considered for comparison purposes since the LTC system dominates the shale matrix response with the response of the HTC system usually embedded in that of the LTC system. The goodness of fit (regression coefficient, R^2) reached 0.92, indicating an excellent fitting result.

In the above table, ε denotes the dielectric permittivity, C_p denotes the specific heat capacity, and λ_l is the heat transfer rate between the two systems.

The temperatures of both systems, both with and without consideration of the heat transfer term, are also shown. As shown in the figure, the heat transfer term increases the temperature of the LTC system at the expense of the HTC system.

5 Results and discussions

In this section, the verified numerical model is applied to investigate the impacts of different parameters on the microwave irradiation process, with the limitations and future work regarding the novel approach outlined. Mesh-dependent convergence is first analyzed. The details are introduced below.

5.1 Mesh-dependent convergence analysis

The element quality exerts an important influence on the convergence and accuracy of finite element analysis. In this section, five scenarios with different mesh element quality (MEQ) were designed for grid-independent analysis as displayed in Table 5. The MEQ in the table is calculated as:

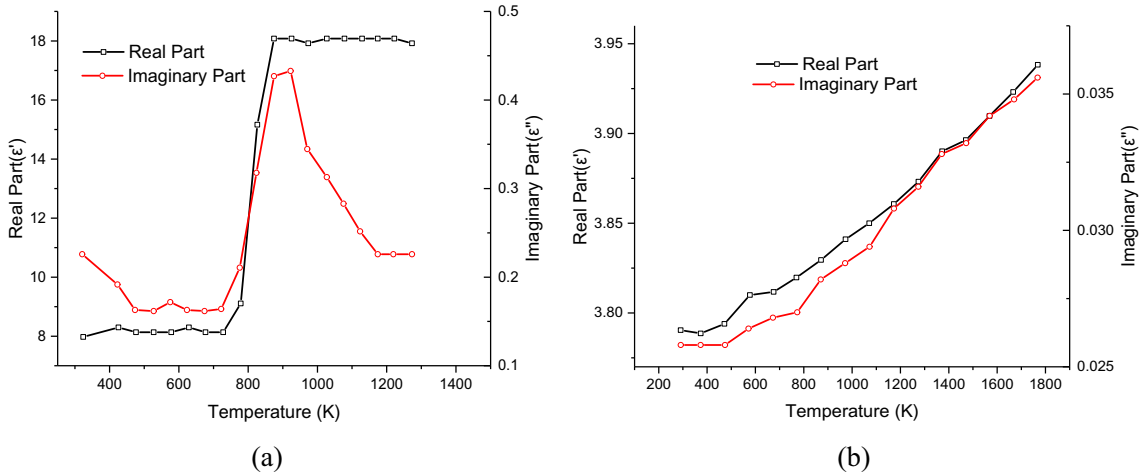

Fig. 9 Assumed relationship of the dielectric permittivity with the temperature: **a** HTC and **b** LTC systems

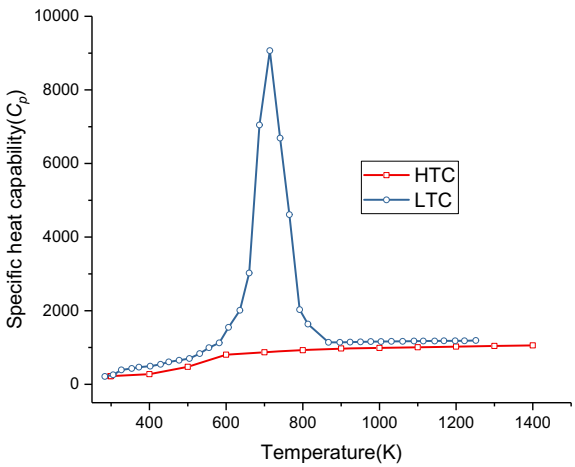

Fig. 10 Relationship of the specific heat capacity with the temperature

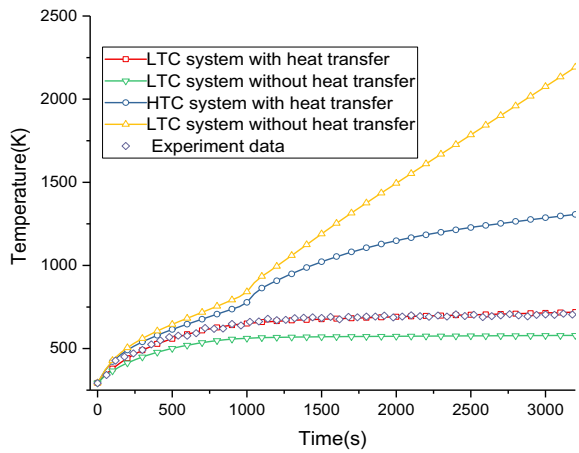

Fig. 11 Comparison of the experimental data and fitted results

Table 4 Parameters for the microwave heating simulations

Component	Value	Component	Value
Microwave frequency	2.45 GHz	Microwave power	700 W
Oven size (cuboid)	329 × 315 × 180 (mm)	Guide size (cuboid)	78 × 50 × 18 (mm)
Sample size (cylinder)	100 × 50 (mm)	Sample density	2600 kg/m^3
Initial temperature	300 K	Dielectric constant of air	1
ε of the HTC system	Figure 9a	ε of the LTC system	Figure 9b
C_p of the HTC system	Figure 10	C_p of the LTC system	Figure 10
Microwave output mode	TE10	λ_l	2000

Table 5 Mesh-independence validation of the geometry model

Element size	Element number	Mesh element quality	Computation time	R^2
Coarser	1707	0.6123	–	
Coarse	3194	0.6519	1 min 44 s	0.7
Normal	48,246	0.6635	5 min 59 s	0.85
Fine	143,795	0.6625	14 min 14 s	0.92
Finer	239,172	0.6619	26 min 10 s	0.93

$$\mathrm{MEQ} = \frac{4\sqrt{3}A}{h_1^2 + h_2^2 + h_3^2} \tag{11}$$

where A denotes the area of the element and h_1, h_2 and h_3 are the side lengths of the triangle.

In the case of a coarser element size, the simulations did not converge, and as a result, the computation time and R^2 value could not be determined. In the remaining four cases, the computation time and temperature increased with the element number and mesh element quality. In the case of a finer element size, the computation time largely increased, with the R^2 value only enhanced by 0.01. Therefore, a fine element size was selected for the following calculation.

5.2 Impact of the heat transfer rate

5.2.1 Three temperature increase stages

As mentioned above, heat transfer increases the temperature of the LTC system and compensates for the temperature of the HTC system. The heat transfer term is proportional to the product of the temperature difference and the newly defined parameter, i.e., the heat transfer coefficient (λ_l). In this section, the impact of the heat transfer coefficient is investigated with values ranging from 1000 to 8000. The temperatures of both the LTC and HTC systems are shown in Fig. 12.. In the following figures, the average value of the whole sample is considered unless stated otherwise.

In regard to the LTC system, the temperature increase process occurs in three stages, with each stage determined from the curve: *(i) A linearly increasing stage:* at this stage, the temperature increases linearly with the irradiation time due to the low specific heat capacity value; *(ii) temperature plateau:* as the temperature reaches a certain threshold value, the temperature remains constant despite a continuous input of energy. At this stage, the absorbed energy mainly contributes to mineral phase transition or water evaporation. *(iii) Rapidly increasing stage:* at this stage, the temperature again increases with the irradiation time as the mineral phase transition process is finished and the specific heat capacity decreases to follow its original increasing trend.

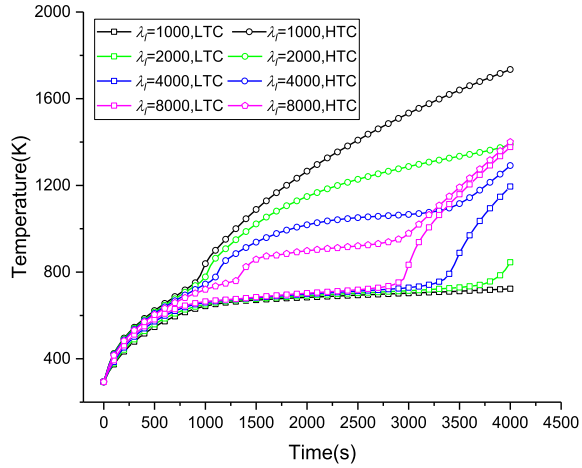

Fig. 12 Variation in the temperatures of the LTC and HTC systems under the different heat transfer coefficients (λ_l)

It should be noted that not all three temperature evolution stages are observed under the different heat transfer coefficients (λ_l). Given a high value of the heat transfer coefficient (λ_l), all three stages are observed for both systems. Conversely, given a low heat transfer coefficient value, only the first two stages (the linearly increasing stage and temperature plateau) are observed for the LTC system, while the first and last stages (the linearly and rapidly increasing stages, respectively) are observed for the HTC system.

5.2.2 *Contributions of the different heat source mechanisms*

As mentioned above, the temperature increase in the LTC system is induced by both microwave dissipation and heat transfer from the HTC system. In this section, the contributions of these two mechanisms and their variations with the heat transfer coefficient (λ_l) are examined, as shown in Fig. 13. In the figure, the total energy is calculated through temperature integration with the specific heat capacity, and the microwave dissipation energy is calculated through time integration with the microwave-supplied heat source (Eq. (2)). The transferred heat energy is the difference between the above two values. The microwave irradiation energy level is consistent across the different cases, as the value varies slightly with the heat transfer coefficient (λ_l).

Figure 13a shows that the level of transferred energy increases with the heat transfer coefficient (λ_l) and is first lower than the microwave irradiation level but then increases with increasing irradiation time. Additionally, Fig. 13b reveals that the proportion of transferred energy increases with the irradiation time and heat transfer coefficient (λ_l). Regarding the proportion of microwave irradiation energy, the opposite situation is observed.

5.3 Impact of the temperature-dependent parameters

In the model verification process, the two key parameters (the dielectric permittivity and specific heat capacity) are both assumed to be temperature-dependent variables. In this section, the impacts of the above two temperature-dependent parameters are investigated. For simplicity, only the effects of the dielectric permittivity on the HTC system and the impact of the specific heat capacity on the LTC system are explored.

5.3.1 *Impact of the dielectric permittivity*

Five scenarios are designed to elucidate the impact of the dielectric permittivity on the temperature increase process. The real part is varied under the first three scenarios, and the imaginary parts are different between the last two scenarios. The details of the designed scenarios are described as follows:

Scenario I: The real and imaginary parts of the dielectric permittivity, as shown in Fig. 9a, are applied in this scenario.

Scenario II: The real part, as shown in Fig. 9a, without the sudden increase after 800 K and the imaginary part, as shown in Fig. 9a, are applied in the calculation.

Scenario III: The real part without the low value before 800 K, as shown in Fig. 9a, and the

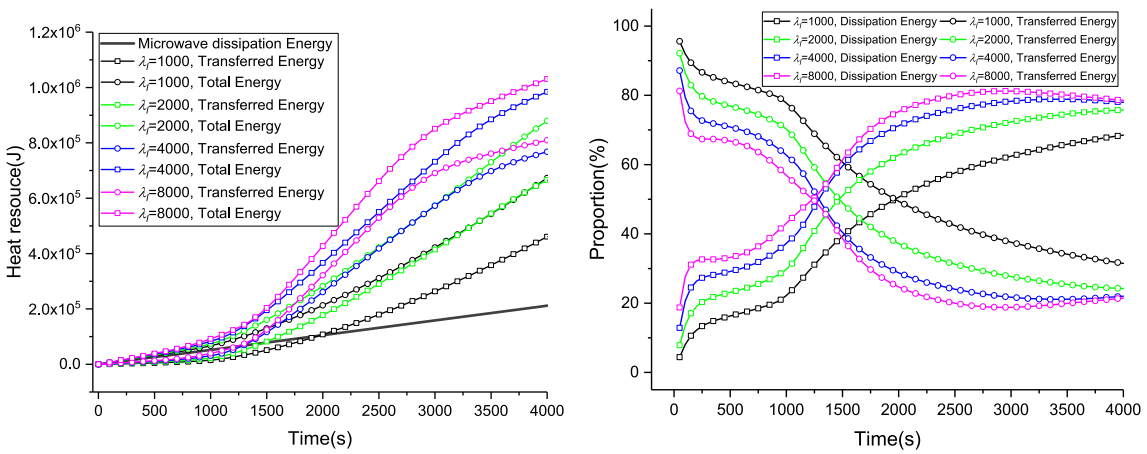

(a) (b)

Fig. 13 **a** Contributions and **b** proportion of the microwave dissipation energy and transferred energy and corresponding variations in the LTC system with the heat transfer coefficient (λ_l)

imaginary part, as shown in Fig. 9a, are applied in this scenario.

Scenario IV: The real part, as shown in Fig. 9a, and the imaginary part, as shown in Fig. 9a, but without the peak are applied in the calculation.

Scenario V: The real part, as shown in Fig. 9a, and the imaginary part, as shown in Fig. 9a, but without the decrease after the peak are applied in this scenario.

The dielectric permittivity values under the five designed scenarios are also shown in Fig. 14a with the results depicted in Fig. 14b. In this section, the average temperature of the whole sample is selected for comparison. The impact of the real part is first investigated by comparing the first three scenarios. As shown in the figure, the temperature is lower than that under Scenario I when ignoring the sudden increase (Scenario II). Additionally, the temperature is higher than that under Scenario I when ignoring the initial relatively low values (Scenario III). It seems that a higher value of the real part results in a higher electric field intensity and therefore a larger temperature increase. However, this response is not universal.

The electric field intensities in the sample under varied real parts are shown in Fig. 15. The real part changes not only the electric field intensity but also the field distribution. Therefore, the average value of the electric field intensity in the shale sample does not always increase with the value of the real part. As shown in the figure, the electric field intensity given a value of 9.10811 of the real part is the highest among the four cases. The impact of the imaginary part could be determined by comparing Scenarios I, IV, and V. A higher value of the imaginary part leads to a greater increase in temperature, which is consistent with Eq. (2).

5.3.2 Impact of the specific heat capacity

Additionally, five scenarios are designed to reveal the impact of the peak value of the specific heat capacity on the temperature-evolution profile. The specific heat capacity values depicted in Fig. 10 with varying peak values are applied under the different designed scenarios, as shown in Fig. 16a, with the results illustrated in Fig. 16b.

As discussed above, the temperature-evolution curve can be divided into three stages. Only the first two stages occur under both Scenarios I and II without the third stage, as shown in Fig. 16b. Under Scenario V, the second stage disappears with the first and third stages occurring. Under Scenarios III and IV, all three stages can be observed, while under Scenario IV, the third stage is rapidly reached. Therefore, we can obtain that: the peak in the specific heat capacity-temperature curve is the main contributor to the second stage (the temperature plateau) of the temperature-evolution curve. The integral value of the specific heat capacity peak and temperature area, as shown in Fig. 16a, represents a trough in the energy potential, and notable energy is required to overcome this stage.

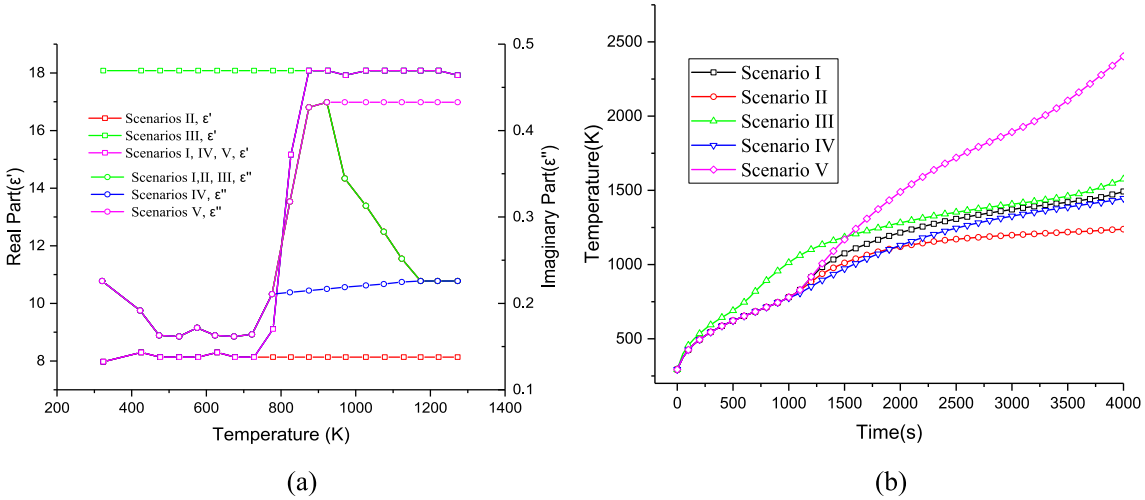

Fig. 14 **a** Dielectric permittivity and **b** temperature variations over time under the five designed scenarios

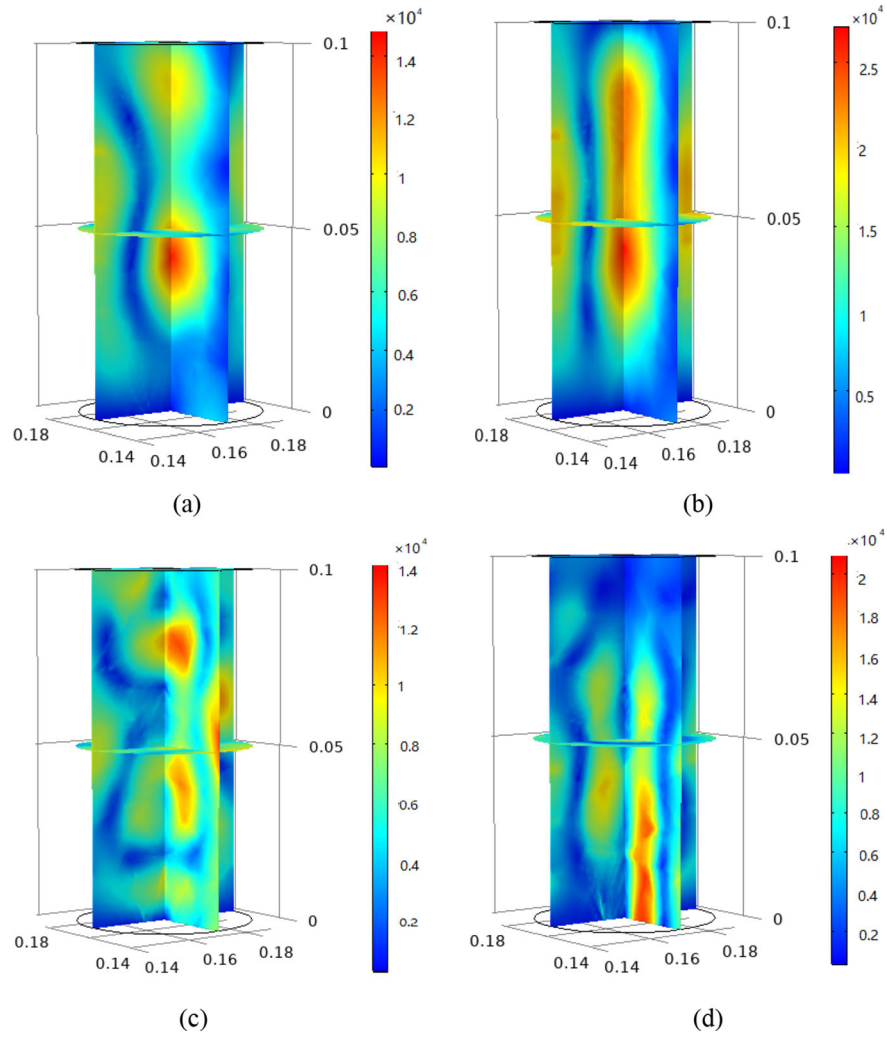

Fig. 15 Evolution of the electric field intensity for real part values of **a** 8.13, **b** 9.11, **c** 15.16 and **d** 18.08

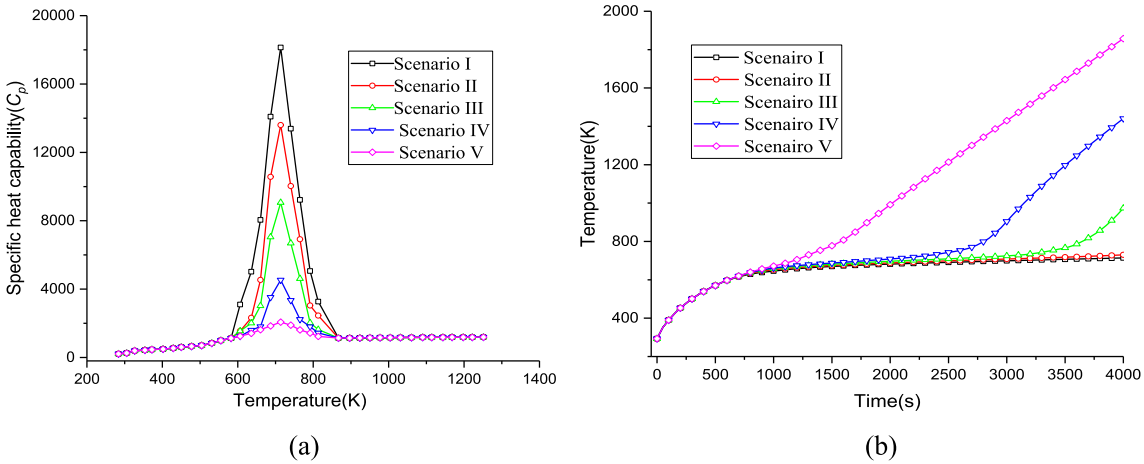

Fig. 16 **a** Determined specific heat capacity and **b** temperature variations over time under the different scenarios

When the absorbed energy is below this value, the temperature-evolution curve occurs at the second stage (the temperature plateau), and when the absorbed energy exceeds this value, the curve progresses into the third stage (the rapidly increasing stage).

5.4 Study limitations and future work

The limitations of the assumptions of the novel simulation approach proposed in this work are discussed, and directions warranting future study are defined.

5.4.1 Limitations of the established approach

As mentioned above, an alternative approach is established to simulate microwave irradiation in strongly heterogeneous rocks with the following limitations:

(a) Mineral aggregate groups.

In this novel approach, the mineral aggregates in the shale matrix are divided into a binary mixture of minerals with either HTC or LTC characteristics with the experimental temperature curve considered for separation, which results in the following limitations: (i) rock exhibits highly heterogeneous and, besides minerals, also contains cracks, grain boundary weaknesses and cleavage planes, which are ignored in the current model; (ii) phase transition and reaction processes of minerals are not fully investigated. In this work, only the phase transition process of quartz is considered, while the phase transition and reaction processes of the other minerals and their impacts are not included. (iii) The transformative capacity of microwave radiation energy into heat varies with increasing temperature between the different minerals. For example, a specific mineral may belong to the LTC component group at a low temperature but transitions into the HTC component group at a higher temperature due to the change in transformative capacity.

(b) Parameter determinations for both systems.

In the simulation process, electromagnetic and thermodynamic parameters are needed for both the HTC and LTC systems. In this work, the related parameters are artificially assumed via fitting of the measured temperature curve. These parameters are difficult to determine since only aggregate parameters for an ensemble sample may be measured in the laboratory.

(c) Heat transfer in the subsystem.

In this novel approach, the two systems interact via heat transfer under the assumption of a pseudosteady state. In this state, the geometric shape and interior structure of each system are ignored, and therefore, the heat transfer process and temperature gradient in the system are neglected. These two factors can affect heat transfer between the two systems based on our knowledge of dual-porosity media (Cui et al. 2020b, c).

(d) Impacts of water and gas.

Most rock types can be categorized into porous media with more or less water occurring in the pore/fracture system. Selecting shale gas reservoirs as an example, a nonnegligible amount of connate water occurs (Xiong et al. 2020; Li et al. 2016). In addition to connate water, more than 50% of the fracturing fluid is retained in shale formations after flowback (Cheng 2012). The dielectric permittivity of water (with an imaginary part value of 12 at 25 °C and 2.45 GHz) (Liu et al. 2020) is much higher than that of rock-forming minerals. In terms of source rock samples with a moderate amount of pore water, after microwave irradiation, the temperature of water in the pores rapidly increases when heating the rock matrix due to energy transfer. In the presence of water or other high-dielectric permittivity liquids (such as oil), the proposed approach remains suitable by choosing water as the HTC system. Under these conditions, the proposed approach is analogous to the classical dual-porosity model, as most water is present in the pore/fracture system.

In addition to water, certain gases are deposited in rocks, such as natural gas reservoirs. The gas stored in rocks can be categorized into the LTC system due to the lower dielectric permittivity and higher specific heat capacity. In most natural gas reservoirs, gas and water molecules coexist in pore/fracture systems. Under these conditions, whether the pore/fracture systems belong to the HTC or LTC system depends on the relative content of water and gas. In most of these cases, we recommend treating the pore/fracture

system as the HTC system because of the higher dielectric permittivity of water.

5.4.2 Future work

(a) Improved coupling processes.

In this work, a preliminary electromagnetic thermal coupling model is established (Fig. 2), but the following improvements are necessary: (i) Coupling of the electromagnetic fields between the HTC and LTC systems. In the current work, this relationship is not considered. The electromagnetic field propagation processes in the HTC and LTC systems are interdependent since polarization in one mineral aggregate affects the electromagnetic propagation process in adjacent aggregates (Smith 1977); (ii) feedback of the heating process to electromagnetic field propagation. In the current work, the temperature-dependent dielectric permittivity is adopted as the mechanism of heating in response to the electromagnetic field. The relationship between the dielectric permittivity and temperature of the minerals is difficult to determine, as individual minerals usually occur on a micrometer scale. (iii) Variation in the heat transfer coefficient (λ_l): in the current work, the heat transfer coefficient (λ_l) is treated as a constant. In fact, this parameter is not a constant but varies with the temperature difference between the two systems and the stress–strain state based on knowledge of analogous dual-porosity media (Cui et al. 2018b, b).

(b) Mechanical interaction between the two systems.

(In this novel approach, the mineral aggregates are divided into two groups, namely, HTC and LTC minerals, considering heat transfer between these groups. The thermal strain developed in each system and the thermal stress resulting from mechanical interaction are ignored. This is a key mechanism for microwave heating-induced fractures or damage and is driven by the different thermal expansion coefficients and nonhomogeneous distribution of the dielectric permittivity of the various minerals (Metaxas and Meredith 1983; Wang and Forssberg 2005). This results in microcracking at the interface between adjacent minerals (intergranular fractures) or within the minerals (transgranular fractures) (Metaxas and Meredith 1983; Wang and Forssberg 2005) and the potential to impact the heat transfer response.

The novel approach provides an alternative method to predict failure modes and fracture types. The thermal stress in each system can be calculated as the product of $K\alpha\Delta T$, where K is the bulk modulus of each system and α denotes the thermal expansion coefficient. A maximum tensile stress criterion can be applied to determine the initiation and progression of transgranular fractures. Additionally, the shear stress along crystal faces can be evaluated as a function of the thermal stress difference between these two systems and their geometric shape. Intergranular fractures can be predicted with a criterion limiting the maximum shear stress.

5.4.3 Implications for field applications

As mentioned above, the application prospects of microwave heating for mechanical excavation in rock projects (Hartlieb et al. 2012; Lu et al. 2017), drilling (Jerby et al. 2002) and energy exploitation (Chen et al. 2021; Cui et al. 2020a) have been extensively studied, both experimentally and numerically. The majority of the simulation works focused on the mineral scale and demonstrated that thermal stress differences between the different minerals could generate new fractures damaging rocks. While limited works focused on the field scale (Gasbarri et al. 2011; Liu et al. 2018), they did not consider the damage process, exact mineralogical composition nor distribution at this large scale.

The proposed approach in this work offers a convenient and efficient way to address the rock damage process at the field scale. The suggested process is as follows: (i) fresh rock blocks should be selected to drill samples with a diameter of 5 cm and a height of 10 cm with offcuts applied for mineral composition measurement; (ii) the sample should then be microwave heated to determine the temperature–time profile, but the irradiation time should be long enough to acquire the whole temperature increase curve; (iii) the dielectric and thermodynamic properties of the two systems should be artificially assumed referring to the corresponding mineral compositions to fit the obtained temperature–time profile; (iv) the two systems and verified parameters should be applied at the field scale to simulate the microwave process, with

the damage process determined as described in Sect. 5.4.2.

6 Conclusions

An effective dual-medium approach is proposed to investigate the microwave heating process in heterogeneous rock, and a coupled electromagnetic-thermal model is established. In this approach, mineral aggregates in the shale matrix are divided into a binary system of either high- or low-transformative capacity (HTC or LTC, respectively) materials coupled by heat transfer. The new approach is verified based on experimentally observed temperature profiles combined with numerical experiments to investigate parameter sensitivities. Furthermore, the limitations and future research prospects of the current work are outlined. Based on the aforementioned results, the following conclusions can be drawn:

(1) The temperature increase in the HTC and LTC systems is affected by both microwave irradiation and heat transfer between the two systems. The heat transfer process, proportional to the heat transfer coefficient (λ_l), increases the temperature of the LTC system and correspondingly decreases the temperature of the HTC system. The proportion of microwave irradiation energy transformed into heat decreases with the irradiation time, while the proportion of transferred energy increases with the irradiation time.

(2) A three-stage temperature-evolution profile is broadly observed in rocks consisting of linearly increasing, stable and rapidly increasing stages. These three stages may not all appear in all rocks, with the temperature–time profile depending on the thermodynamic composition. The peak in the specific heat capacity-temperature curve, resulting from temperature-dependent mineral phase transition or water evaporation, is the main contributor to the temperature plateau over time under a continued EM irradiative input. Additionally, in the case of a high heat transfer coefficient, all three stages can be observed for both systems, while in the case of a low heat transfer coefficient, not all three stages occur.

(3) The impact of the real part of the dielectric permittivity is not universal since the real part not only influences the value of the electric field intensity but also the field distribution. Conversely, the impact of the imaginary part is determined, with a higher value resulting in a larger increase in temperature.

(4) The limitations of the current work and required future work are also outlined. The division of the mineral aggregates and parameter determinations for both systems are two limiting factors of the application of the proposed approach. The mechanical interactions between these two systems and the completion of the coupling process are two urgent tasks that should be addressed since the former term provides the key mechanism for microwave heating-induced fracturing or damage. Additionally, the latter term could enhance the coupling model and yield more accurate results. Implications of the proposed approach for field applications are further examined with a feasible process recommended.

Acknowledgements This research was supported by the Natural Science Foundation of China (Grant No. 12002081), China Postdoctoral Science Foundation (Grant No. 2019M661118), and the "111" Project (Grant No. B17009).

Declarations

Conflict of interest On behalf of all authors, the corresponding author states that there is no conflict of interest.

References

Ali AY, Bradshaw SM (2010) Bonded-particle modelling of microwave-induced damage in ore particles. Miner Eng 23(10):780–790. https://doi.org/10.1016/j.mineng.2010.05.019

Aqil S, Schmitt DR (2010) Dielectric permittivity of clay adsorbed water: effect of salinity. Geo Conv 2010:1–4

Bera A, Babadagli T (2017) Effect of native and injected nanoparticles on the efficiency of heavy oil recovery by radio frequency electromagnetic heating. J Pet Sci Eng 153:244–256. https://doi.org/10.1016/j.petrol.2017.03.051

Bobicki ER, Liu Q, Xu Z (2014) Microwave heating of ultramafic nickel ores and mineralogical effects. Miner Eng 58:22–25. https://doi.org/10.1016/j.mineng.2014.01.003

Chandrasekaran S, Basak T, Srinivasan R (2013) Microwave heating characteristics of graphite based powder mixtures.

Int Commun Heat Mass 48:22–27. https://doi.org/10.1016/j.icheatmasstransfer.2013.09.008

Chen TT, Dutrizac JE, Haque KE, Wyslouzil W, Kashyap S (1984) The relative transparency of minerals to microwave radiation. Can Metall Q 23(3):349–351. https://doi.org/10.1179/cmq.1984.23.3.349

Chen T, Feng XT, Cui G, Tan Y, Pan Z (2019) Experimental study of permeability change of organic-rich gas shales under high effective stress. J Nat Gas Sci Eng 64:1–14. https://doi.org/10.1016/j.jngse.2019.01.014

Chen T, Zheng X, Qiu X, Feng XT, Pan Z (2021) Experimental study on the feasibility of microwave heating fracturing for enhanced shale gas recovery. J Nat Gas Sci Eng 6:104073. https://doi.org/10.1016/j.jngse.2021.104073

Cheng Y (2012) Impact of water dynamics in fractures on the performance of hydraulically fractured wells in gas-shale reservoirs. J Can Pet Technol 51(02):143–151. https://doi.org/10.2118/127863-PA

Church RH, Webb WE, Salsman J (1988) Dielectric properties of low-loss minerals.US Department of the Interior.

COMSOL M (2018) Application libraries. Version 5.4, Comsol

Corradi AB, Leonelli C, Manfredini T, Pennisi L, Romagnoli M (1996) Quantitative determination of pyrite in, ceramic clay raw materials by DTA. Thermochim Acta 287(1):101–109. https://doi.org/10.1016/0040-6031(96)02984-X

Cui G, Liu J, Wei M, Feng X, Elsworth D (2018a) Evolution of permeability during the process of shale gas extraction. J Nat Gas Sci Eng 49:94–109. https://doi.org/10.1016/j.jngse.2017.10.018

Cui G, Liu J, Wei M, Shi R, Elsworth D (2018b) Why shale permeability changes under variable effective stresses: new insights. Fuel 213:55–71. https://doi.org/10.1016/j.fuel.2017.10.068

Cui G, Chen T, Feng XT, Chen Z, Elsworth D, Yu H, Zheng X, Pan Z (2020a) Coupled multiscale-modeling of microwave-heating-induced fracturing in shales. Int J Rock Mech Min 136:104520. https://doi.org/10.1016/j.ijrmms.2020.104520

Cui G, Feng XT, Pan Z, Chen T, Liu J, Elsworth D, Tan Y, Wang C (2020b) Impact of shale matrix mechanical interactions on gas transport during production. J Pet Sci Eng 184:106524. https://doi.org/10.1016/j.petrol.2019.106524

Cui G, Tan Y, Chen T, Feng XT, Elsworth D, Pan Z, Wang C (2020c) Multidomain two-phase flow model to study the impacts of hydraulic fracturing on shale gas production. Energy Fuel 34(4):4273–4288. https://doi.org/10.1021/acs.energyfuels.0c00062

Cumbane AJ (2003) Microwave treatment of minerals and ores. University of Nottingham

Deyab SM, Rafezi H, Hassani F, Kermani M, Sasmito AP (2021) Experimental investigation on the effects of microwave irradiation on kimberlite and granite rocks. J Rock Mech Geotech Eng 13(2):267–274. https://doi.org/10.1016/j.jrmge.2020.09.001

Dirisu JO, Fayomi OS, Oyedepo SO (2019) Thermal emission and heat transfer characteristics of ceiling materials: a necessity. Eng Procedia 157:331–342. https://doi.org/10.1016/j.egypro.2018.11.198

Farag S, Sobhy A, Akyel C, Doucet J, Chaouki J (2012) Temperature profile prediction within selected materials heated by microwaves at 2.45 GHz. Appl Therm Engg 36:360–369. https://doi.org/10.1016/j.applthermaleng.2011.10.049

Flesoura G, Garcia-Banos B, Catala-Civera JM, Vleugels J, Pontikes Y (2019) In-situ measurements of high-temperature dielectric properties of municipal solid waste incinerator bottom ash. Ceram Int 45(15):18751–18759. https://doi.org/10.1016/j.ceramint.2019.06.101

Ford JD, Pei DC (1967) High temperature chemical processing via microwave absorption. J Microw Power 2(2):61–64. https://doi.org/10.1080/00222739.1967.11688647

Gasbarri S, Diaz A, Guzman M (2011) Evaluation of electric heating on recovery factors in extra heavy oil reservoirs. In: SPE heavy oil conference and exhibition

Haque KE (1999) Microwave energy for mineral treatment processes—a brief review. Int J Miner Process 57(1):1–24. https://doi.org/10.1016/S0301-7516(99)00009-5

Hartlieb P, Leindl M, Kuchar F, Antretter T, Moser P (2012) Damage of basalt induced by microwave irradiation. Miner Eng 31:82–89. https://doi.org/10.1016/j.mineng.2012.01.011

Hartlieb P, Toifl M, Kuchar F, Meisels R, Antretter T (2016) Thermo-physical properties of selected hard rocks and their relation to microwave-assisted comminution. Miner Eng 91:34–41. https://doi.org/10.1016/j.mineng.2015.11.008

Hartlieb P, Kuchar F, Moser P, Kargl H, Restner U (2018) Reaction of different rock types to low-power (3.2 kW) microwave irradiation in a multimode cavity. Miner Eng 118:37–51. https://doi.org/10.1016/j.mineng.2018.01.003

Hascakir B, Akin S (2009) Recovery of Turkish oil shales by electromagnetic heating and determination of the dielectric properties of oil shales by an analytical method. Energy Fuel 24(1):503–509. https://doi.org/10.1021/ef900868w

Jerby E, Dikhtyar V, Aktushev O, Grosglick U (2002) The microwave drill. Science 298(5593):587–589. https://doi.org/10.1126/science.1077062

Jiajia C, Krishnamoorthy P, Sohan B, Mehrdad N, David J, Jeyamkondan S (2015) Heat and mass transport during microwave heating of mashed potato in domestic oven-model development, validation, and sensitivity analysis. J Food Sci 79(10):E1991–E2004. https://doi.org/10.1111/1750-3841.12636

Jones DA (2005) Understanding microwave treatment of ores. Doctor, University of Nottingham

Jones DA, Lelyveld T, Mavrofidis S, Kingman S, Miles N (2002) Microwave heating applications in environmental engineering-a review. Resour Conserv Recycl 34(2):75–90. https://doi.org/10.1016/S0921-3449(01)00088-X

Jones DA, Kingman SW, Whittles DN, Lowndes IS (2007) The influence of microwave energy delivery method on strength reduction in ore samples. Chem Eng Process 46(4):291–299. https://doi.org/10.1016/j.cep.2006.06.009

Josh M, Clennell B (2015) Broadband electrical properties of clays and shales: comparative investigations of remolded and preserved samplesBroadband electrical properties of clay. Geophysics 80(2):D129–D143. https://doi.org/10.1190/geo2013-0458.1

Kingman S, Vorster W, Rowson N (2000) The influence of mineralogy on microwave assisted grinding. Miner Eng

13(3):313–327. https://doi.org/10.1088/0022-3727/10/4/004

Li J, Li X, Wu K, Wang X, Shi J, Yang L, Zhang H, Sun Z, Wang R, Feng D (2016) Water sorption and distribution characteristics in clay and shale: effect of surface force. Energy Fuel 30(11):8863–8874. https://doi.org/10.1021/acs.energyfuels.6b00927

Li H, Shi S, Lin B, Lu J, Lu Y, Ye Q, Wang Z, Hong Y, Zhu X (2019a) A fully coupled electromagnetic, heat transfer and multiphase porous media model for microwave heating of coal. Fuel Process Technol 189:49–61. https://doi.org/10.1016/j.fuproc.2019.03.002

Li J, Kaunda RB, Arora S, Hartlieb P, Nelson PP (2019ab) Fully-coupled simulations of thermally-induced cracking in pegmatite due to microwave irradiation. J Rock Mech Geotech 11(2):242–250. https://doi.org/10.1016/j.jrmge.2018.12.007

Li X, Wang S, Xu Y, Yao W, Xia K, Lu G (2020) Effect of microwave irradiation on dynamic mode-I fracture parameters of Barre granite. Eng Fract Mech. https://doi.org/10.1016/j.engfracmech.2019.106748

Liu HP, Chen TP, Li Y, Song ZY, Wang SW, Wu SH (2016) Temperature rise characteristics of ZhunDong coal during microwave pyrolysis. Fuel Process Technol 148:317–323. https://doi.org/10.1016/j.fuproc.2016.03.017

Liu J, Wang J, Leung C, Gao F (2018) A fully coupled numerical model for microwave heating enhanced shale gas recovery. Energies 11(6):1608. https://doi.org/10.3390/en11061608

Liu J, Liang X, Xue Y, Yao K, Fu Y (2020) Numerical evaluation on multiphase flow and heat transfer during thermal stimulation enhanced shale gas recovery. Appl Therm Eng. https://doi.org/10.1016/j.applthermaleng.2020.115554

Lovás M, Kováčová M, Dimitrakis G, Čuvanová S, Znamenáčková I, Jakabský Š (2010) Modeling of microwave heating of andesite and minerals. Int J Heat Mass Tran 53(17–18):3387–3393. https://doi.org/10.1016/j.ijheatmasstransfer.2010.03.012

Lu GM, Li YH, Hassani F, Zhang X (2017) The influence of microwave irradiation on thermal properties of main rock-forming minerals. Appl Therm Eng 112:1523–1532. https://doi.org/10.1016/j.applthermaleng.2016.11.015

McGill S, Walkiewicz J, Smyres G (1988) The effects of power level on the microwave heating of selected chemicals and minerals. MRS Online Proc Libr Arch. https://doi.org/10.1557/PROC-124-247

Meisels R, Toifl M, Hartlieb P, Kuchar F, Antretter T (2015) Microwave propagation and absorption and its thermo-mechanical consequences in heterogeneous rocks. Int J Miner Process 135:40–51. https://doi.org/10.1016/j.minpro.2015.01.003

Metaxas AA, Meredith RJ (1983) Industrial microwave heating, IET

Nicco M, Holley EA, Hartlieb P, Kaunda R, Nelson PP (2018) Methods for characterizing cracks induced in rock. Rock Mech Rock Eng 51(7):2075–2093. https://doi.org/10.1007/s00603-018-1445-x

Onwude DI, Hashim N, Abdan K, Janius R, Chen G, Kumar C (2018) Modelling of coupled heat and mass transfer for combined infrared and hot-air drying of sweet potato. J Food Eng 228:12–24. https://doi.org/10.1016/j.jfoodeng.2018.02.006

Peinsitt T, Kuchar F, Hartlieb P, Moser P, Kargl H, Restner U, Sifferlinger NA (2010) Microwave heating of dry and water saturated basalt, granite and sandstone. Int J Min Miner Eng 2(1):18-29(12). https://doi.org/10.1504/IJMME.2010.031810

Pickles CA (2004) Microwave heating behaviour of nickeliferous limonitic laterite ores. Miner Eng 17(6):775–784. https://doi.org/10.1016/j.mineng.2004.01.007

Pitchai K, Chen J, Birla S, Gonzalez R, Jones D, Subbiah J (2014) A microwave heat transfer model for a rotating multi-component meal in a domestic oven: development and validation. J Food Eng 128:60–71. https://doi.org/10.1016/j.jfoodeng.2013.12.015

Simpkin R (2010) Derivation of lichtenecker's logarithmic mixture formula from Maxwell's equations. IEEE Trans Microw Theory 58(3):545–550. https://doi.org/10.1109/TMTT.2010.2040406

Skauge A, Fuller N, Hepler LG (1983) Specific heats of clay minerals: sodium and calcium kaolinites, sodium and calcium montmorillonites, illite, and attapulgite. Thermochim Acta 61(1):139–145. https://doi.org/10.1016/0040-6031(83)80310-4

Smith GB (1977) Dielectric constants for mixed media. J Phys D Appl Phys 10(4):L39. https://doi.org/10.1088/0022-3727/10/4/004

Tahmasebi A, Yu J, Li X, Meesri C (2011) Experimental study on microwave drying of Chinese and Indonesian low-rank coals. Fuel Process Technol 92(10):1821–1829. https://doi.org/10.1016/j.fuproc.2011.04.004

Toifl M, Meisels R, Hartlieb P, Kuchar F, Antretter T (2016) 3D numerical study on microwave induced stresses in inhomogeneous hard rocks. Miner Eng 90:29–42. https://doi.org/10.1016/j.mineng.2016.01.001

Toifl M, Hartlieb P, Meisels R, Antretter T, Kuchar F (2017) Numerical study of the influence of irradiation parameters on the microwave-induced stresses in granite. Miner Eng 103–104:78–92. https://doi.org/10.1016/j.mineng.2016.09.011

Tuncer E, Gubański SM, Nettelblad B (2001) Dielectric relaxation in dielectric mixtures: application of the finite element method and its comparison with dielectric mixture formulas. J Appl Phys 89(12):8092–8100. https://doi.org/10.1063/1.1372363

Ulaby FT, Bengal TH, Dobson MC, East JR, Garvin JB, Evans DL (1990) Microwave dielectric properties of dry rocks. IEEE Trans Geosci Remote Sens 28(3):325–336. https://doi.org/10.1109/36.54359

Wang Y, Djordjevic N (2014) Thermal stress FEM analysis of rock with microwave energy. Int J Miner Process 130:74–81. https://doi.org/10.1016/j.minpro.2014.05.012

Wang Y, Forssberg E (2005) Dry comminution and liberation with microwave assistance. Scand J Metall 34(1):57–63. https://doi.org/10.1111/j.1600-0692.2005.00718.x

Wen T, Zhao Y, Xiao Q, Ma Q, Kang S, Li H, Song S (2017) Effect of microwave-assisted heating on chalcopyrite leaching of kinetics, interface temperature and surface energy. Results Phys 7:2594–2600. https://doi.org/10.1016/j.rinp.2017.07.035

Xiong H, Devegowda D, Huang L (2020) Water bridges in clay nanopores: mechanisms of formation and impact on

hydrocarbon transport. Langmuir 36(3):723–733. https://doi.org/10.1021/acs.langmuir.9b03244

Yamada T, Ueda T, Kitayama T (1982) Piezoelectricity of a high-content lead zirconate titanate/polymer composite. J Appl Phys 53(6):4328. https://doi.org/10.1063/1.331211

Yu H, Li Y, Cui G, Elsworth D, Liu J, Liu M (2021) A model for focused-beam microwave heating on rock fracturing. Geomech Geophys Geo-Energy Georesour 7(2):1–22. https://doi.org/10.1007/s40948-021-00242-9

Yuan Y, Shao Z, Qiao R, Fei X, Cheng J (2020) Thermal response and crack propagation of mineral components in olivine basalt under microwave irradiation. Arab J Geosci-Czech. https://doi.org/10.1007/s12517-020-05494-5

Zakri T, Laurent JP, Vauclin M (1998) Theoretical evidence for 'Lichtenecker's mixture formulae' based on the effective medium theory. J Phys D Appl Phys 31(13):1589. https://doi.org/10.1088/0022-3727/31/13/013

Zhang XG, Ranjith PG, Perera MS, Ranathunga AS, Haque A (2016) Gas transportation and enhanced coalbed methane recovery processes in deep coal seams: a review. Energy Fuel 30(11):8832–8849. https://doi.org/10.1021/acs.energyfuels.6b01720

Zheng Y, Wang S, Feng J, Ouyang Z, Li X (2005) Measurement of the complex permittivity of dry rocks and minerals: application of polythene dilution method and Lichtenecker's mixture formulae. Geophys J Int 163(3):1195–1202. https://doi.org/10.1111/j.1365-246X.2005.02718.x

Zhou Y, Li E, Guo G, Gao Y, Yang T (2011) Broadband complex permittivity measurement of low loss materials over large temperature ranges by stripline resonator cavity using segmentation calculation method. Prog Electromagn Res. https://doi.org/10.2528/PIER10112402